

Femtometer Toroidal Structures in Nuclei

J. L. Forest* and V. R. Pandharipande†

Department of Physics, University of Illinois at Urbana-Champaign, Urbana, IL 61801

Steven C. Pieper‡ and R. B. Wiringa§

Physics Division, Argonne National Laboratory, Argonne, IL 60439

R. Schiavilla¶

CEBAF Theory Group, Newport News, VA 23606,

and

Department of Physics, Old Dominion University, Norfolk, VA 23529

A. Arriaga**

Centro de Fisica Nuclear da Universidade de Lisboa, Avenida Gama Pinto 2, 1699 Lisboa,

Portugal

(December 27, 2013)

Abstract

The two-nucleon density distributions in states with isospin $T = 0$, spin $S=1$ and projection $M_S=0$ and ± 1 are studied in ${}^2\text{H}$, ${}^3,4\text{He}$, ${}^6,7\text{Li}$ and ${}^{16}\text{O}$. The equidensity surfaces for $M_S=0$ distributions are found to be toroidal in shape, while those of $M_S=\pm 1$ have dumbbell shapes at large density. The dumbbell shapes are generated by rotating tori. The toroidal shapes indicate that the tensor correlations have near maximal strength at $r < 2$ fm in all these nuclei. They provide new insights and simple explanations of the structure and electromagnetic form factors of the deuteron, the quasi-deuteron model, and the dp , dd and αd $L=2$ (D -wave) components in ${}^3\text{He}$, ${}^4\text{He}$ and ${}^6\text{Li}$. The toroidal distribution has a maximum-density diameter of ~ 1 fm and a half-maximum density thickness of ~ 0.9 fm. Many realistic models of nuclear forces predict these values, which are supported by the observed electromagnetic form factors of the deuteron, and also predicted by classical Skyrme effective Lagrangians, related to QCD in the limit of infinite colors. Due to the rather small size of this structure, it could have a revealing relation to certain aspects of QCD. Experiments to probe this structure and its effects in nuclei are suggested. Pair distribution functions in other T, S channels are also discussed; those in $T, S = 1, 1$ have anisotropies expected from one-pion exchange interactions. The tensor correlations in $T, S = 0, 1$ states are found to deplete the number of $T, S = 1, 0$ pairs in nuclei and cause a reduction in nuclear binding energies via many-body effects.

PACS numbers: 21.30.+y, 21.45.+v

I. INTRODUCTION

Nuclear structure has been discussed mostly in the context of the liquid drop and shell models. These models have been extremely useful in explaining many observed nuclear properties. However, they are based on macroscopic concepts, and do not address the simplest nuclei, hydrogen and helium. Furthermore, recent $(e, e'p)$ experiments [1] have indicated that in heavier near-closed-shell nuclei, less than 70% of the nucleons are in the single-particle orbitals that would be fully occupied in the simple shell model.

To obtain a more microscopic description of nuclear structure, we may regard the nucleus as a collection of interacting nucleons described by the Hamiltonian [2]

$$H = \sum_i -\frac{\hbar^2}{2m} \nabla_i^2 + \sum_{i<j} v_{ij} + \sum_{i<j<k} V_{ijk}. \quad (1.1)$$

The interactions v_{ij} and V_{ijk} are not exactly known, but v_{ij} is well constrained by the available scattering data, and binding energies and theoretical considerations place important constraints on V_{ijk} . The structure of the ground-state wave function Ψ_0 at small interparticle distances is influenced by the repulsive core and tensor parts of v_{ij} . Most realistic models of v_{ij} contain these components and, for example, the Reid [3], Paris [4], Urbana [5] and new Argonne v_{18} [6] models seem to predict similar structures. The three-nucleon interaction V_{ijk} is much weaker than the v_{ij} . Due to a large cancellation between kinetic and two-body interaction energies, it has a significant effect on nuclear binding energies [2] but its effect on the structure of Ψ_0 is much less than that of the better known v_{ij} .

Due to the strong spin-isospin dependence of v_{ij} and V_{ijk} it is difficult to solve the Schrödinger equation with the Hamiltonian (1.1). Only recently it has been possible to obtain accurate solutions for $A \leq 7$ nuclei [7,8] with the Green's Function Monte Carlo (GFMC) method. Accurate variational wave functions Ψ_v , which contain less than 0.5% admixture of excited states are known for $A = 3$ and 4 nuclei [9]. The available Ψ_v for ${}^6,7\text{Li}$ [10] and ${}^{16}\text{O}$ [11,12] are certainly not as accurate as those for $A = 3$ and 4, nevertheless they presumably contain most of the important structure of the Ψ_0 .

In this paper we examine the short-range structure of ${}^2\text{H}$, ${}^3,4\text{He}$, ${}^6,7\text{Li}$ and ${}^{16}\text{O}$ by calculating the two-nucleon density distributions in states with isospin T , spin S , and spin projection M_S . Since the deuteron has only two nucleons, its one- and two-body density distributions are trivially related. Variational wave functions Ψ_v and Monte Carlo methods are used for $A > 2$.

The two-nucleon distributions in the $T, S = 0, 1$ states have a strong dependence on the spin projection M_S . The equidensity surfaces, spanning the top three quarters of the density range in $M_S=0$ states, have toroidal shape. These tori are produced by the joint action of the repulsive core and tensor interactions. In contrast the equidensity shapes in the $M_S=\pm 1$ have dumbbell shapes, which have been studied earlier in the deuteron [13,14]. A brief description of the two-nucleon interaction in $T, S = 0, 1$ states is given in section II, and the density distribution of the deuteron is discussed in detail in section III, where we show that the dumbbell-shaped distributions in $M_S=\pm 1$ states are produced by rotating tori. Commonly used models of v_{ij} predict that the maximum density torus has a diameter of ~ 1 fm, and the half-maximum density torus has a thickness of ~ 0.9 fm. In section III we relate these dimensions of the toroidal distribution to the observed electromagnetic form factors of the deuteron. The structures are rather dense; current models predict the maximum one-body density of the torus inside the deuteron to be $\sim 0.34 \pm 0.02 \text{ fm}^{-3}$, i.e., approximately twice nuclear matter density.

The two-nucleon $T, S = 0, 1$, $M_S = 0, \pm 1$ density distributions in ${}^3,4\text{He}$, ${}^6,7\text{Li}$ and ${}^{16}\text{O}$ are compared with those of the deuteron in section IV. The distributions for $r < 2$ fm differ only by a single scale factor. They indicate that in the $T = 0$ state, the tensor correlations have near maximal strength for $r < 2$ fm in all these nuclei. The scale factor is identified as the Levinger-Bethe quasi-deuteron number, and its value is compared to the ratios of total photon ($E_\gamma = 80$ to 120 MeV) and pion ($E_{\pi^+} \sim 115$ MeV) absorption cross sections.

In order to study the nature of many-body structures induced by these compact two-body structures we study the dp , dd and αd overlaps with the Ψ_v of ${}^3\text{He}$, ${}^4\text{He}$ and ${}^6\text{Li}$ in section V. These depend strongly on the spin projection M_d of the deuteron and indicate the

presence of anisotropic structures in all these nuclei. Experiments to probe these structures are suggested.

Pair distribution functions in other T, S, M_S states are discussed in section VI. Those in $T, S = 1, 1, M_S = 0, \pm 1$ states are anisotropic as expected from the pion-exchange tensor force. We also find that the number of $T, S = 1, 0$ pairs in a nucleus is reduced due to many-body effects involving the strong $T, S = 0, 1$ tensor correlations. This reduction gives a significant contribution to the saturation of nuclear binding energies.

The Skyrme field theory [15], related to QCD in the limit of large number of colors $N_c \rightarrow \infty$, has predicted toroidal shapes for the deuteron [16–18] in the classical limit. Density distributions of the ground states with 3 to 6 baryons have also been calculated [19] in this limit. In the last section, VII, we summarize our results, obtained with conventional nuclear many-body theory, and indicate their relation to those of the Skyrme field theory in the classical limit, and of the constituent quark model.

II. THE TWO-NUCLEON INTERACTION IN THE $T, S = 0, 1$ STATE

Nuclear forces are not yet quantitatively understood from QCD. However, many realistic models have been constructed by fitting the available two-nucleon scattering data. The shape of the short-range structures in the $T, S = 0, 1$ state appears to be relatively model-independent. The interaction $v_{0,1}$ in the $T, S = 0, 1$ state in Reid, Urbana and Argonne models can be expressed as

$$v_{0,1} = v_{0,1}^c(r) + v_{0,1}^t(r)S_{ij} + v_{0,1}^{ls}(r)\mathbf{L} \cdot \mathbf{S} + v_{0,1}^{l2}(r)L^2 + v_{0,1}^{ls2}(r)(\mathbf{L} \cdot \mathbf{S})^2, \quad (2.1)$$

while a ∇^2 operator is used instead of L^2 in the Paris potential. The structures are formed mostly by the static part of the interaction:

$$v_{0,1}^{stat} = v_{0,1}^c(r) + v_{0,1}^t(r)S_{ij}. \quad (2.2)$$

It is instructive to study the expectation values of $v_{0,1}^{stat}$ in eigenstates of the position operator \mathbf{r} with spin projections $M_S=0$ and $M_S=\pm 1$. These depend upon r and θ , the polar angle of

\mathbf{r} with respect to the spin-quantization axis \hat{z} , and are given by

$$\langle M_S=0 | v_{0,1}^{stat}(\mathbf{r}) | M_S=0 \rangle = v_{0,1}^c(r) - 4v_{0,1}^t(r)P_2(\cos \theta), \quad (2.3)$$

$$\langle M_S=\pm 1 | v_{0,1}^{stat}(\mathbf{r}) | M_S=\pm 1 \rangle = v_{0,1}^c(r) + 2v_{0,1}^t(r)P_2(\cos \theta). \quad (2.4)$$

The $M_S=0$ expectation value of $v_{0,1}^{stat}$ has the largest variation with θ as illustrated in Fig. 1. The static potential has a repulsive core; outside the core it is very attractive for $\theta=\pi/2$ and repulsive for $\theta=0$ and π . Therefore, in this state the np pairs form a toroidal density distribution in the xy plane. The potential in the $M_S=\pm 1$ states is attractive for $\theta=0$ and π , and equal to that for $M_S=0$, $\theta=\pi/2$, while it is repulsive for $\theta=\pi/2$ and half way between the $M_S=0$, $\theta=0$ and $\pi/2$ potentials. Thus the $M_S=\pm 1$ potential has two distinct minima separated by a barrier, and therefore the density distributions have a dumbbell shape in this state.

At $r > 1.5$ fm, the $v_{0,1}^{stat}$ is dominated by the one-pion-exchange potential, while at smaller r it has a significant model dependence. Much of this model dependence is cancelled by the differences in the momentum-dependent terms in the models. In particular, the deuteron wave functions calculated from these potentials have much smaller model dependence. These are commonly written as

$$\Psi_d^{M_d}(\mathbf{r}) = R_0(r) \mathcal{Y}_{011}^{M_d}(\hat{r}) + R_2(r) \mathcal{Y}_{211}^{M_d}(\hat{r}), \quad (2.5)$$

where $R_0(=u/r)$ and $R_2(=w/r)$ are the S - and D -state radial wave functions and \mathcal{Y}_{LSJ}^M are the spin-angle functions. The R_0 and R_2 calculated from the different potential models are shown in Fig. 2. The short-range structures are related to the R_0 and R_2 functions, and therefore we expect them to be fairly model-independent.

However, the ‘‘full’’ Bonn potential [20] offers an exception. The R_0 and R_2 predicted by this one-boson-exchange model of the NN interaction are similar to other predictions at larger r , but they have an additional sharp structure with a range of ~ 0.2 fm. We will not consider the possibility of such an additional structure in this work.

III. THE DEUTERON

The short-range structure of the deuteron is most obvious in its density distribution $\rho_d^{M_d}(r', \theta)$ which depends upon the projection M_d of the total deuteron angular momentum, the distance r' from the deuteron center of mass, and the polar angle θ of \mathbf{r}' ; it is independent of the azimuthal angle ϕ . Note that the interparticle distance $\mathbf{r} = 2\mathbf{r}'$, and the standard normalizations,

$$\int_0^\infty r^2 dr [R_0^2(r) + R_2^2(r)] = 1, \quad (3.1)$$

$$\int d^3\mathbf{r}' \rho_d^{M_d}(\mathbf{r}') = 2, \quad (3.2)$$

are used in this work.

The $\rho_d^{M_d}(\mathbf{r}')$ is given by $16\Psi_d^{M_d^\dagger}(2\mathbf{r}')\Psi_d^{M_d}(2\mathbf{r}')$, where the factor 16 comes from the difference in normalizations (3.1) and (3.2). A simple calculation using Eq. (2.5) yields

$$\rho_d^0(\mathbf{r}') = \frac{4}{\pi} [C_0(2r') - 2C_2(2r')P_2(\cos\theta)] \quad , \quad (3.3)$$

$$\rho_d^{\pm 1}(\mathbf{r}') = \frac{4}{\pi} [C_0(2r') + C_2(2r')P_2(\cos\theta)] \quad , \quad (3.4)$$

with

$$C_0(r) = R_0^2(r) + R_2^2(r) \quad , \quad (3.5)$$

$$C_2(r) = \sqrt{2}R_0(r)R_2(r) - \frac{1}{2}R_2^2(r) \quad . \quad (3.6)$$

The interesting structure of these density distributions is shown in Figs. 3-6. Fig. 3 shows $\rho_d^{M_d}(r')$ along $\theta = 0$ and $\theta = \pi/2$ directions, noting that

$$\rho_d^0(r', \theta=\pi/2) = \rho_d^{\pm 1}(r', \theta=0). \quad (3.7)$$

The above densities are the largest while $\rho_d^0(r', \theta=0)$ is the smallest as expected from the properties of $v_{0,1}^{stat}$ discussed in Sec. II. The small value of the ratio $\rho_d^0(r', \theta=0)/\rho_d^0(r', \theta=\pi/2)$ indicates that the deuteron has near maximal tensor correlation at distance $r' < 1$ fm or equivalently at $r < 2$ fm. This ratio is ~ 0 for maximal tensor correlations.

Figures 4 and 5 show the density distributions predicted by the Argonne v_{18} model in the $x'z'$ plane. The maximum value of ρ_d is fairly model-independent (Fig. 3) and large (~ 0.35 fm $^{-3}$). The maxima of ρ_d^0 (Fig. 4) form a ring with a diameter of ~ 1 fm, denoted by d , in the $x'y'$ plane, while the $\rho_d^{\pm 1}$ has two equal maxima on the z' -axis (Fig. 5) at $z' = \pm d/2$.

The three-dimensional distributions $\rho_d^{M_d}(\mathbf{r}')$ can be obtained by rotating the distributions shown in Figs. 4 and 5 about the z' -axis. They are represented by equidensity surfaces shown in Fig. 6 for $\rho_d = 0.24$ and 0.08 fm $^{-3}$; all four sections are drawn to the same scale. The maximum value of $\rho_d^0(\theta=0)$ is ~ 0.05 fm $^{-3}$ (Fig. 3). Therefore the equidensity surfaces for ρ_d^0 having $\rho_d > 0.05$ fm $^{-3}$ cannot intersect the z' -axis, and thus have toroidal shapes shown in Figs. 6B and 6D. The central hole in these tori is due to the repulsive core in $v_{0,1}^{stat}$, and their angular confinement is due to the tensor force. In absence of the tensor force, $R_2(r) = 0$, the $\rho_d^0 = \rho_d^{\pm 1}$, and the equidensity surfaces are concentric spheres.

The maximum value of $\rho_d^{\pm 1}(\theta=\pi/2)$ is ~ 0.19 fm $^{-3}$ as can be seen from Fig. 3. Therefore the equidensity surfaces of $\rho_d^{\pm 1}$ for $\rho_d \geq 0.19$ fm $^{-3}$ can not cross the $\theta=\pi/2$ plane; they have two disconnected parts forming a dumbbell as shown in Fig. 6A. At smaller values of ρ_d we also obtain two equidensity $\rho_d^{\pm 1}$ surfaces (Fig. 6C), consisting of an inner surface due to the repulsive core enclosed by an outer. At very small ρ_d (≤ 0.05 fm $^{-3}$) the equidensity surfaces of ρ_d^0 also have disconnected inner and outer parts, neither close to spherical in shape.

The toroidal shape of the $M_d=0$ equidensity surfaces is more compact and persists down to smaller ρ_d , or equivalently to larger values of r' , as can be seen from Figs. 3-6. In the classical Skyrmion field theory only this shape is obtained for the distribution of baryon density in the ground state for two baryons [15]. The deuteron can be considered to be more deformed in the $M_d=0$ state. For example, the expectation values of the quadrupole operator $Q(\mathbf{r}') = 2 r'^2 P_2(\cos \theta)$ obey the relation

$$\int \rho_d^0(\mathbf{r}') Q(\mathbf{r}') d^3\mathbf{r}' = -2 \int \rho_d^{\pm 1}(\mathbf{r}') Q(\mathbf{r}') d^3\mathbf{r}'. \quad (3.8)$$

It is rather simple to obtain the $\rho_d^{\pm 1}(\mathbf{r}')$ from the $\rho_d^0(\mathbf{r}')$. We rotate the $\rho_d^0(\mathbf{r}')$ about the y' -axis by an angle of $\pi/2$ so that the toroidal ring is in $y'z'$ plane with x' as the symmetry

axis. This places the deuteron in the superposition of $M_d=\pm 1$ states. The $M_d=\pm 1$ states are obtained by spinning the rotated toroid about the z' -axis, and the $\rho_d^{\pm 1}(\mathbf{r}')$ is just the average value of the density of the spinning toroid, i.e.,

$$\rho_d^{\pm 1}(r', \theta) = \frac{1}{2\pi} \int_0^{2\pi} \rho_d^0(r', \cos^{-1}(\sin \theta \cos \phi)) d\phi. \quad (3.9)$$

The $L=1, M=\pm 1$ states of the harmonic oscillator, given by $\phi(r)=e^{-\nu r^2}(x\pm iy)$, are obtained in the same way from the $\phi(r)=e^{-\nu r^2}z$, $L=1, M=0$ state. Therefore it is tempting to consider the toroidal shape of ρ_d^0 as the basic shape of the deuteron. The expectation value of the current operator is zero in the $M_d=0$ state, therefore one may regard that as the “static” state of the deuteron. Note that the toroidal shapes cannot be obtained by rotating the dumbbell by $\pi/2$ about the y' -axis and spinning it about the z' -axis. This gives $\rho_d^0(\theta=0, r') = \rho_d^{\pm 1}(\theta=\pi/2, r')$ which is not true. The dumbbell- or cigar-shaped density distribution of the deuteron in the $M_d=\pm 1$ state has been studied earlier [13,14]. Unfortunately the toroidal distribution of the $M_d=0$ state was not studied, and its similarity with the predictions of Skyrminion field theory was not noticed.

The deuteron electromagnetic structure functions $A(q)$ and $B(q)$, and the tensor polarization $T_{20}(q)$ in elastic electron-deuteron scattering have been extensively studied experimentally [21–30] and theoretically [31–34]. They are usually calculated from the S - and D -wave functions R_0 and R_2 obtained from realistic interactions, by including in the nuclear electromagnetic current, in addition to the dominant impulse approximation (IA) operators, relativistic corrections and two-body meson-exchange contributions [31,33]. More recently, calculations of these observables based on quasipotential reductions of the Bethe-Salpeter equation and one-boson-exchange interaction models, constrained to fit nucleon-nucleon data, have also been carried out [32,34]. The theoretical predictions for the structure functions based on both the nonrelativistic and relativistic approaches are in good agreement with data. Our interest here is not to improve upon the present theoretical predictions, but to relate the values of the minima and maxima of $T_{20}(q)$ and $B(q)$ to the size of the toroidal structure in the deuteron. The q -values of these extrema may be shifted by $\sim 10\%$

by corrections to the impulse approximation used in the following pedagogical analysis.

The charge form factors, defined as

$$F_{C,M_d}(q) = \frac{1}{2} \int \rho_d^{M_d}(\mathbf{r}') e^{iqz'} d^3\mathbf{r}', \quad (3.10)$$

are shown in Fig. 7. At large q the $F_{C,1}(q)$ gets most of its contribution from the two peaks of $\rho_d^1(\mathbf{r}')$ (Fig. 5) at $z'=\pm d/2$. The Fourier transform of the sum of two δ -functions at $z'=\pm d/2$ is given by $\cos(qd/2)$ with zeros at $qd=\pi, 3\pi, \dots$. These zeros are due to the cancellation of the contribution from the two peaks, and they persist even when the peaks have a finite width. The first two minima of $F_{C,1}^2(q)$, obtained from the Argonne v_{18} $\rho_d^1(\mathbf{r}')$, occur at $q_1=3.6$ and $q_2=12.6$ fm $^{-1}$. The effective values d_i estimated from the minima q_i , using $d_i=(2i-1)\pi/q_i$, are 0.87 and 0.75 fm for $i=1, 2$. These values are smaller than the diameter $d=1$ fm because the dumbbell ends (Fig. 6A) are not spherical. Nevertheless the minima of $F_{C,1}^2$ seem to be primarily determined by the diameter d of the maximum-density torus.

The Fourier transforms of a disc of thickness t , with \mathbf{q} perpendicular to the disc, are proportional to $\sin(qt/2)/(qt/2)$ irrespective of the shape of the disc. These have zeros at $qt=2\pi, 4\pi, \dots$, which may be used to obtain the thickness t . The first two zeros of $F_{C,0}(q)$ at $q=9.2$ and 19.5 fm $^{-1}$ (Fig. 7) give values 0.68 and 0.64 fm for the effective thickness of the torus. The maximum thickness along the z -axis of the calculated equidensity surface at half maximum density is 0.88 fm.

The $T_{20}(q)$ form factor of the deuteron has small magnetic contributions which depend upon the electron scattering angle θ . The extrema of T_{20} are not significantly affected by this magnetic contribution as can be seen from Fig. 8, and ignoring it we obtain a rather simple equation:

$$T_{20}(q) \sim -\sqrt{2} \frac{F_{C,0}^2(q) - F_{C,1}^2(q)}{F_{C,0}^2(q) + 2F_{C,1}^2(q)}. \quad (3.11)$$

Its minima occur when $F_{C,1}^2(q)=0$, while the maxima have $F_{C,0}^2(q)=0$. These minima and maxima correspond to those values of q at which the recoiling deuteron has only $M_d=0$

or $M_d = \pm 1$, respectively. The first minimum of T_{20} is experimentally known to occur at $q \sim 3.5 \pm 0.5 \text{ fm}^{-1}$ in agreement with the value $d \sim 1 \text{ fm}$ predicted by realistic potentials. The first maximum of T_{20} has not yet been experimentally located; it provides a measure of the thickness t .

In magnetic elastic scattering the deuteron spin projection M_d in the \mathbf{q} direction changes by ± 1 since the photon has $M_\gamma = \pm 1$. Thus the magnetic form factor $F_M(q)$ is a transition form factor. It has convection current and spin-flip terms [31,33] of which the latter is dominant. The $F_M(q)$ calculated with and without the convection current term are not too different (Fig. 9). The spin flip part of $F_M(q)$ can be obtained from the transition density $\rho_{tr}(\mathbf{r}')$:

$$F_M^{sf}(q) = (\mu_p + \mu_n) \int e^{iqz'} \rho_{tr}(\mathbf{r}') d^3 \mathbf{r}', \quad (3.12)$$

$$\rho_{tr}(\mathbf{r}') = \frac{2}{\pi} \left\{ R_0^2(2r') - \frac{1}{2} R_2^2(2r') - \frac{1}{2} \left[\sqrt{2} R_0(2r') R_2(2r') + R_2^2(2r') \right] P_2(\cos \theta) \right\}. \quad (3.13)$$

This transition density is shown in Fig. 10; it is dominated by the toroidal $\rho_d^0(\mathbf{r}')$, and its effective thickness along z' axis, obtained from the zeros of $F_M(q)$ (Fig. 9), is $\sim 0.85 \text{ fm}$. The minimum of $F_M(q)$ is observed [26] at $q \sim 7 \text{ fm}^{-1}$, supporting the theoretical estimates of t .

The deuteron wave function in momentum space is defined as

$$\begin{aligned} \tilde{\Psi}_d^{M_d}(\mathbf{k}) &= \frac{1}{(2\pi)^{3/2}} \int d^3 \mathbf{r} e^{-i\mathbf{k}\cdot\mathbf{r}} \Psi_d^{M_d}(\mathbf{r}) \\ &= \tilde{R}_0(k) \mathcal{Y}_{011}^{M_d}(\hat{\mathbf{k}}) + \tilde{R}_2(k) \mathcal{Y}_{211}^{M_d}(\hat{\mathbf{k}}) \quad , \end{aligned} \quad (3.14)$$

with

$$\tilde{R}_L(k) = i^L \sqrt{2/\pi} \int_0^\infty dr r^2 j_L(kr) R_L(r) \quad . \quad (3.15)$$

The momentum distributions $\tilde{\rho}_d^{M_d}(\mathbf{k})$, given by $\tilde{\Psi}_d^{M_d^\dagger}(\mathbf{k}) \tilde{\Psi}_d^{M_d}(\mathbf{k})$, are then easily obtained as

$$\tilde{\rho}_d^0(\mathbf{k}) = \frac{1}{4\pi} \left[\tilde{C}_0(k) - 2\tilde{C}_2(k) P_2(\cos \theta_k) \right] \quad , \quad (3.16)$$

$$\tilde{\rho}_d^{\pm 1}(\mathbf{k}) = \frac{1}{4\pi} \left[\tilde{C}_0(k) + \tilde{C}_2(k) P_2(\cos \theta_k) \right] \quad , \quad (3.17)$$

where θ_k is the angle between \mathbf{k} and \hat{z} -axis, and the $\tilde{C}_L(k)$ are defined as in Eqs. (3.5)-(3.6) with $R_L(r)$ replaced by $\tilde{R}_L(k)$. Note that the $\tilde{\rho}_d$ are normalized such that

$$\int d^3\mathbf{k} \tilde{\rho}_d^{M_d}(\mathbf{k}) = 1 \quad . \quad (3.18)$$

The momentum distributions $\tilde{\rho}_d^0(k, \theta_k)$ and $\tilde{\rho}_d^{\pm 1}(k, \theta_k)$ for $\theta_k = 0$ and $\pi/2$ are shown in Fig. 11. Note that

$$\tilde{\rho}_d^0(k, \theta_k=\pi/2) = \tilde{\rho}_d^{\pm 1}(k, \theta_k=0) \quad . \quad (3.19)$$

The zeros of $\tilde{\rho}_d^{\pm 1}(k, \theta_k=0)$ and $\tilde{\rho}_d^0(k, \theta_k=0)$ occur at $k \simeq 1.5 \text{ fm}^{-1}$ and 5.2 fm^{-1} , respectively, and are related to the spatial dimensions of the torus. In naive estimates these minima occur at $\pi/2d$ and π/t , respectively. Thus measuring the positions of the zeros in these momentum distributions would provide an independent estimate of the spatial dimensions of the toroidal structure in the deuteron. This information would be complementary to that yielded by elastic form factors measurements.

The momentum distributions $\tilde{\rho}_d^{M_d}(k, \theta_k)$ could in principle be measured by $(e, e'p)$ scattering on polarized deuterons. In the one-photon exchange approximation the $\vec{d}(e, e'p)n$ cross section, in the laboratory frame, is generally expressed as

$$\frac{d^5\sigma^{M_d}}{dE'_e d\Omega'_e d\Omega_p} = \sigma_{Mott} p_p E_p R_{\text{rec}}^{-1} (v_L R_L + v_T R_T + v_{LT} R_{LT} + v_{TT} R_{TT}) \quad , \quad (3.20)$$

$$R_{\text{rec}} = \frac{E_p E_n}{m^2} \left| 1 - \frac{E_p p_n}{E_n p_p} \hat{\mathbf{p}}_p \cdot \hat{\mathbf{p}}_n \right| \quad , \quad (3.21)$$

where M_d is the target spin projection, E'_e and Ω'_e are the energy and solid angle of the final electron, and Ω_p is the solid angle of the ejected proton. The coefficients v_α are defined in terms of the electron variables, while the structure functions R_α involve matrix elements

$$\langle n + p; \mathbf{p}_n \mathbf{p}_p, M_n M_p \mid O_{L,T}(\mathbf{q}) \mid d, M_d \rangle \quad , \quad (3.22)$$

of the charge (O_L) and current (O_T) operators between the initial deuteron and final $n + p$ states. The neutron momentum is $\mathbf{p}_n = \mathbf{q} - \mathbf{p}_p$, \mathbf{q} is the momentum transfer, $\mathbf{p}_m = -\mathbf{p}_n$ is the missing momentum, and M_p and M_n are the proton and neutron spin projections, respectively [33]. The cross section for unpolarized deuterons,

$$\frac{d^5\sigma}{dE'_e d\Omega'_e d\Omega_p} = \frac{1}{3} \sum_{M_d=0,\pm 1} \frac{d^5\sigma^{M_d}}{dE'_e d\Omega'_e d\Omega_p} \quad , \quad (3.23)$$

has been measured up to $p_m \sim 500$ MeV/c, and there is good agreement between theory and experiment [35].

In plane-wave-impulse-approximation (PWIA), obtained by neglecting interaction effects in the final $n + p$ states as well as relativistic corrections and two-body terms in the charge and current operators, the M_d -dependent cross section is proportional to

$$\frac{d^5\sigma^{M_d}}{dE'_e d\Omega'_e d\Omega_p} \propto \tilde{\rho}_d^{M_d}(\mathbf{p}_m) \quad . \quad (3.24)$$

Using, for example, tensor polarized deuterium, it should be possible to measure the difference between $\tilde{\rho}_d^0(\mathbf{p}_m)$ and $\tilde{\rho}_d^{\pm 1}(\mathbf{p}_m)$, and therefore empirically determine the positions of the minima in these momentum distributions. Clearly, such an analysis is justified if the PWIA is valid. This assumption has been tested by carrying out the full and PWIA calculations of the $d^5\sigma^{M_d}/dE'_e d\Omega'_e d\Omega_p$ in parallel kinematics with q fixed at 500 MeV/c, ω in the range 290-390 MeV, and the electron scattering angle $\theta_e = 10^\circ$. The results, shown in Fig. 12, indicate that, while FSI, two-body current, and relativistic corrections are not entirely negligible, at least in the kinematical region which has been studied here, their effect is small compared to the difference between the cross sections for $M_d=0$ and ± 1 . We therefore conclude that the results of such an experiment could be used to empirically study the diameter and thickness of the torus. One might argue that this information could be more easily obtained from elastic form factors measurements, as discussed above. However, it should be realized that, in contrast to the $d(e, e')\vec{d}$ data, the double-coincidence data would allow us to ascertain to what extent this toroidal structure is due to nucleonic degrees of freedom.

IV. THE TWO-NUCLEON DENSITY DISTRIBUTIONS IN NUCLEI

The two-nucleon density-distributions in T , S , M_T , M_S two-nucleon states are defined as

$$\rho_{T,S}^{M_T, M_S}(\mathbf{r}) = \frac{1}{2J+1} \sum_{M_J=-J}^J \langle \Psi^{M_J} | \sum_{i<j} P_{ij}(\mathbf{r}, T, S, M_T, M_S) | \Psi^{M_J} \rangle \quad . \quad (4.1)$$

Here $|\Psi^{M_J}\rangle$ denotes the ground state of the nucleus with total angular momentum J and projection M_J , and $P_{ij}(\mathbf{r}, T, S, M_T, M_S)$ projects out the specific two-nucleon state with $\mathbf{r}_i - \mathbf{r}_j = \mathbf{r}$. For $N = Z$ nuclei, the wave functions used in this study are symmetric under exchange of neutrons and protons; hence $\rho_{T,S}^{M_T, M_S}(\mathbf{r})$ is independent of M_T . For ${}^3\text{He}$, we have

$$\rho_{1,S}^{-1, M_S} = 0; \quad \rho_{1,S}^{+1, M_S} = 2\rho_{1,S}^{0, M_S} \quad , \quad (4.2)$$

while for larger $N \neq Z$ nuclei, the M_T dependence is nontrivial. In the following we discuss $\rho_{T,S}^{M_S}$, the average over M_T of $\rho_{T,S}^{M_T, M_S}$. The $\rho_{T,S}^{M_S}$ is normalized such that

$$\sum_{T,S,M_S} (2T+1) \int \rho_{T,S}^{M_S}(\mathbf{r}) d^3\mathbf{r} = \frac{1}{2}A(A-1) \quad , \quad (4.3)$$

which is the number of pairs in the nucleus. It is a function of r and θ independent of the azimuthal angle ϕ .

It can be verified from Eqs.(3.3-3.6) and (4.1) that in the deuteron

$$\rho_{0,1}^M(\mathbf{r}) = \frac{1}{3} \times \frac{1}{16} \rho_d^M(\mathbf{r}' = \mathbf{r}/2) \quad . \quad (4.4)$$

Note that the spin-dependent two-body density on the left ($M_S = M$) is an average over projections M_d in the deuteron, while the polarized one-body density on the right ($M_d = M$) has been summed over spins. The $\rho_{T,S}^{M_S}$ in ${}^3,4\text{He}$, ${}^6,7\text{Li}$, and ${}^{16}\text{O}$ have been calculated from variational wave functions using Monte Carlo techniques. For the $A \leq 7$ nuclei, these wave functions minimize the expectation value of a Hamiltonian consisting of the Argonne v_{18} two-nucleon and Urbana IX three-nucleon potentials [7] (for $A = 6,7$ the minimization is constrained by the experimental rms radii); a detailed description of the form of the wave functions is given in Refs. [9,10]. The wave function for ${}^{16}\text{O}$ was obtained from the variationally best wave function by slightly increasing the radius of the single-particle part of the wave function so as to reproduce the experimental rms radius of ${}^{16}\text{O}$. The details of the ${}^{16}\text{O}$ wave function will be published elsewhere [12]. A cluster-expansion including up to four-body clusters with Monte Carlo integration [11] was used to compute the two-body densities in ${}^{16}\text{O}$.

To reduce statistical fluctuations in the calculation, we write

$$\rho_{T,S}^{M_S}(\mathbf{r}) = \sum_{L=0,2} A_{T,S,L}^{M_S}(r) P_L(\cos\theta) \quad , \quad (4.5)$$

and directly compute the $A(r)$ as

$$A_{T,S,L}^{M_S}(r) = \frac{1}{2J+1} \frac{2L+1}{4\pi} \times \sum_{M_J} \int d\mathbf{R} \Psi^{M_J}(\mathbf{R})^\dagger \sum_{i<j} \frac{1}{r_{ij}^2} \delta(r - r_{ij}) P_L(\hat{\mathbf{r}}_{ij} \cdot \hat{\mathbf{z}}) P_{ij}(T, S, M_S) \Psi^{M_J}(\mathbf{R}) \quad , \quad (4.6)$$

where \mathbf{R} represents the coordinates $\mathbf{r}_1, \dots, \mathbf{r}_A$. Because of the average over the total spin of the nucleus, the $A_{T,S,L}^{M_S}$ are zero for $L > 2$, and

$$A_{T,S=1,L=0}^{M_S=0} = A_{T,S=1,L=0}^{M_S=\pm 1} \quad , \quad (4.7)$$

$$A_{T,S=1,L=2}^{M_S=0} = -2A_{T,S=1,L=2}^{M_S=\pm 1} \quad . \quad (4.8)$$

For the deuteron, the $A_{0,1,L}^{M_S}$ are related to the C_L of Eqs.(3.3-3.6) by $A_{0,1,0}^{M_S} = C_0/48$; $A_{0,1,2}^1 = C_2/48$.

The shapes of $\rho_{0,1}^{M_S}(r, \theta)$ are very similar at $r \leq 2$ fm in all the nuclei considered. In order to study the evolution of $\rho_{0,1}^{M_S}$ with A we divided the $\rho_{0,1}^{M_S}(r, \theta)_A$ by the ratio R_{Ad} defined as

$$R_{Ad} = \frac{\text{Max}(\rho_{0,1}^{\pm 1}(r, \theta)_A)}{\text{Max}(\rho_{0,1}^{\pm 1}(r, \theta)_d)} \quad . \quad (4.9)$$

The densities so normalized are compared in Fig. 13, and the values of R_{Ad} are listed in Table I. Fig. 13 shows $\rho_{0,1}^0(r, \theta = 0)_A/R_{Ad}$, $\rho_{0,1}^{\pm 1}(r, \theta = \pi/2)_A/R_{Ad}$, and $\rho_{0,1}^0(r, \theta = \pi/2)_A/R_{Ad}$ for ${}^2\text{H}$, ${}^4\text{He}$, and ${}^{16}\text{O}$. Note that $\rho_{0,1}^0(r, \theta = \pi/2) = \rho_{0,1}^{\pm 1}(r, \theta = 0)$ by virtue of equations (4.4), (4.6) and (4.7) in all nuclei. After normalization by R_{Ad} , the various densities for ${}^3\text{He}$ lie between those of ${}^2\text{H}$ and ${}^4\text{He}$, while those for ${}^6, {}^7\text{Li}$ are in between the ${}^4\text{He}$ and ${}^{16}\text{O}$ results. It is obvious from Fig. 13 that the equidensity surfaces of the two-body density $\rho_{0,1}^{M_S}$ are very similar to those of the deuteron density shown in figures 3-6 at $r < 2$ fm ($r' < 1$ fm). At $r < 2$ fm the ratio $\rho_{0,1}^0(r, \theta = 0)/\rho_{0,1}^0(r, \theta = \pi/2)$ is very small, indicating that the tensor correlations have near maximal strength in all the nuclei considered. In ${}^{16}\text{O}$ the $\rho_{0,1}^{M_S}$ becomes approximately independent of M_S only for $r \gtrsim 3$ fm.

Bethe and Levinger suggested in 1950 [36] that at small distances the relative $T, S = 0, 1$ neutron-proton wave function in a nucleus is likely to be similar to that in the deuteron. We find that this is a good approximation. The expectation value of any short-ranged two-body operator that is large only in the $T, S = 0, 1$ state scales as R_{Ad} . In Table I we list values of the ratios of the calculated expectation values of the one-pion exchange part of the Argonne v_{18} potential, the observed low-energy (118 MeV for ${}^3\text{He}$ [37] and ${}^4\text{He}$ [38], and 115 MeV for ${}^{16}\text{O}$ [39]) pion absorption cross sections and the average value of the observed photon absorption cross sections in the range $E_\gamma = 80$ to 120 MeV. All these processes are dominated by the $T, S = 0, 1$ pairs, and seem to scale as R_{Ad} .

While comparing these ratios in detail it should be realized that $\langle v_\pi \rangle$ in nuclei has a relatively small contribution from $T, S \neq 0, 1$ states, absent in the deuteron, which makes $\langle v_\pi \rangle_A / \langle v_\pi \rangle_d$ slightly larger than R_{Ad} . The $\langle v_\pi \rangle_d = -21.3$ MeV for the Argonne v_{18} model, and it accounts for most of the deuteron potential energy, $\langle v \rangle_d = -22.1$ MeV. Also in larger nuclei, the $\langle v_\pi \rangle_A$ gives a large fraction of the total two-body interaction energy [11]. Direct comparison of the ratio of pion absorption cross sections with R_{Ad} may not be strictly valid. The scattering and absorption of pions by spectator nucleons, absent in the deuteron, is expected to reduce the ratio $\sigma_{ab,A}^\pi / \sigma_{ab,d}^\pi$, while three-body and higher absorption mechanisms, also absent in the deuteron, will increase it. After correcting for final state interactions of the two outgoing protons, the two-body (π^+, pp) part is estimated to account for $\sim 76\%$ of the total absorption cross section for 115 MeV π^+ by ${}^{16}\text{O}$ [39]. In ${}^3\text{He}$ $\sim 20\%$ of the 118 MeV π^+ absorption cross section has three-body character [37], however a part of this 20% must be due to initial and final state interactions.

Results of Mainz experiments [40] on ${}^7\text{Li}$ and ${}^{16}\text{O}$ are used to calculate the average value of σ^γ in the energy interval $E_\gamma = 80$ to 120 MeV. The $\sigma_{ab,d}^\gamma$ averaged over the same energy interval is ~ 0.072 mb [41]. The only available data for ${}^3\text{He}$ in this energy range are from the experiments done in the 1960's [42] and 1970's [43]. The average cross section of the two-body photodisintegration of ${}^3\text{He}$, in the energy range 80-120 MeV, is ~ 0.03 mb [43], and that for the three-body process is ~ 0.10 mb [42], giving total cross section of ~ 0.13 mb.

The average cross section for total absorption of photons by ${}^4\text{He}$ in the same energy range is crudely estimated from Fig. 1 in ref. [44] to be ~ 0.3 mb.

The total number of pairs with given T, S in nuclei can be computed as

$$\begin{aligned} N_{T,S}^A &= \sum_{M_S} (2T + 1) 2\pi \int r^2 dr d\cos\theta \rho_{T,S}^{M_S}(r, \theta)_A \\ &= (2T + 1)(2S + 1) 4\pi \int r^2 dr A_{T,S,0}^0(r) ; \end{aligned} \quad (4.10)$$

the values for $T, S = 0, 1$ and the corresponding naive independent-particle model values are also shown in Table I. We see that the correlations induced by the potentials do not significantly change the $N_{0,1}^A$ from their independent-particle (IP) values; however, as will be discussed later, this is not true for $T=1$ pairs. For few-body nuclei, R_{Ad} is significantly larger than $N_{0,1}^A$, however, in ${}^{16}\text{O}$ $N_{0,1}^A$ has a large contribution from pairs with large r and R_{Ad} is smaller than $N_{0,1}^A$. The calculated value of R_{Ad} for ${}^{16}\text{O}$ is much smaller than Levinger's estimate $R_{Ad} \sim 8NZ/A$ [36].

The $\rho_d^{M=0}(r, \theta = \pi/2)$ has its half-maximum value at $r \sim 1.8$ fm (Fig. 13). If we identify the region with $r < 1.8$ fm as the ‘‘quasi-deuteron’’, then the probability that the np pair in a deuteron is in the quasi-deuteron region is ~ 0.25 , and the number of quasi-deuterons in a nucleus is $\sim R_{Ad}/4$. In the past, however, R_{Ad} itself has been interpreted as the number of quasi-deuterons in the nucleus.

V. TWO-CLUSTER DISTRIBUTION FUNCTIONS

The strong spin-dependent anisotropies of the two-nucleon densities suggest that three-nucleon and higher distribution functions in nuclei could also be anisotropic. A general study of these higher distributions is beyond the scope of this work; however the two-cluster distribution functions $\vec{d}\vec{p}$ in ${}^3\text{He}$, $\vec{d}\vec{d}$ in ${}^4\text{He}$, and $\alpha\vec{d}$ in ${}^6\text{Li}$ are simple to study with the Monte Carlo method [45]. They provide some information on the higher distribution functions, and may be relatively accessible by $(e, e'\vec{d})$ and $(e, e'\vec{p})$ experiments.

The two-cluster overlap function can be written generally as

$$\begin{aligned}
A_{ab}(M_a, M_b, M_J, \mathbf{r}_{ab}) &= \langle \mathcal{A} \Psi_a^{M_a} \Psi_b^{M_b}, \mathbf{r}_{ab} | \Psi^{M_J} \rangle \\
&= \sum_{LM_L SM_S} \langle LM_L SM_S | JM_J \rangle \langle J_a M_a J_b M_b | SM_S \rangle R_L(r_{ab}) Y_{LM_L}(\hat{r}_{ab}),
\end{aligned} \tag{5.1}$$

where \mathbf{r}_{ab} is the relative coordinate between the centers of mass of the two clusters and \mathcal{A} is an antisymmetrization operator for the two-cluster state. The $R_L(r_{ab})$ radial functions can be evaluated from

$$\begin{aligned}
R_L(r_{ab}) &= \sum_{M_a M_b M_L M_S} \langle J_a M_a J_b M_b | SM_S \rangle \langle LM_L SM_S | JM_J \rangle \\
&\int d\mathbf{R} [\mathcal{A} \Psi_a^{M_a}(\mathbf{R}_a) \Psi_b^{M_b}(\mathbf{R}_b)]^\dagger Y_{LM_L}^*(\hat{r}_{ab}) \frac{\delta(r - r_{ab})}{r_{ab}^2} \Psi^{M_J}(\mathbf{R}),
\end{aligned} \tag{5.2}$$

where $\mathbf{R}_{a(b)}$ represents the coordinates of particles in cluster $a(b)$. We note that in PWIA the $(e, e'\vec{a})\vec{b}$ cross section is proportional to the momentum distribution $|\tilde{A}_{ab}(M_a, M_b, M_J, \mathbf{k})|^2$ obtained from the Fourier transform of the overlap function $A_{ab}(M_a, M_b, M_J, \mathbf{r}_{ab})$.

In the present work, the integrations have been made with Monte Carlo techniques akin to Ref. [45], but with some improvements. Configurations are sampled with the weight function $|\Psi_v^{M_J}|^2$ containing the full variational wave function. In Ref. [45] only a single term in the antisymmetric product in Eq. (5.2) is calculated. The efficiency of the Monte Carlo sampling has been improved by evaluating all possible partitions of the nucleus into clusters a and b at each configuration \mathbf{R} . We also use a much larger sample of configurations than in the previous calculations.

We can define a two-cluster wave function, in analogy with the deuteron wave function of Eq. (2.5), using the radial overlap functions

$$\begin{aligned}
\Psi_{ab}^{M_J}(\mathbf{r}_{ab}) &= \sum_{LS} R_L(r_{ab}) \mathcal{Y}_{LSJ}^{M_J}(\hat{r}_{ab}) \\
&= \sum_{M_a M_b} A_{ab}(M_a, M_b, M_J, \mathbf{r}_{ab}) \chi^{M_a} \chi^{M_b},
\end{aligned} \tag{5.3}$$

where χ^{M_a} and χ^{M_b} denote spin states $J_a M_a$ and $J_b M_b$ of a and b . For the cases $ab = dp$, dd , and ad there are both S- and D-wave states in the two-cluster wave function. In these cases the well known D_2 parameter can be defined by means of the $R_0(r)$ and $R_2(r)$ radial functions [46]:

$$D_2^{ab} = \frac{\int R_2(r_{ab})r_{ab}^4 dr_{ab}}{15 \int R_0(r_{ab})r_{ab}^2 dr_{ab}} . \quad (5.4)$$

Although in the present paper we emphasize the short-range structure of nuclei, it is also interesting to study the asymptotic behavior of the overlap radial functions. Of particular interest is the asymptotic D/S ratio $\eta_{ab} = C_2^{ab}/C_0^{ab}$, where C_0 and C_2 are the asymptotic normalization constants of $R_0(r)$ and $R_2(r)$ respectively:

$$R_L(r_{ab}) = \lim_{r_{ab} \rightarrow \infty} -i^L C_L^{ab} h_L(i\alpha_{ab}r_{ab}). \quad (5.5)$$

Here h_L is the spherical Hankel function of first kind and α_{ab} is the wave number associated with the separation energy of the nucleus into clusters a and b . We must point out that the present variational method, as well as the GFMC method, determine the wave functions by energy minimization, to which long-range configurations contribute very little. Therefore these methods are not very sensitive to the asymptotic part of the wave functions, and consequently our values for η_{ab} should be considered only as estimates.

The two-cluster density distribution for a given set of spin projections is defined as:

$$\rho_{ab}^{M_a, M_b, M_J}(\mathbf{r}_{ab}) = |A_{ab}(M_a, M_b, M_J, \mathbf{r}_{ab})|^2. \quad (5.6)$$

In each of the cases studied here, it exhibits spin-dependent spatial anisotropies which are easily understood in terms of the toroidal or dumbbell structure of the polarized deuteron. The density is enhanced in the direction corresponding to the most efficient or compact placement of the deuteron with the remaining cluster, and reduced in those directions that would lead to very extended structures.

Finally, we are also interested in the total normalizations N_L of the S- and D-wave two-cluster distributions:

$$N_L^{ab} = \int_0^\infty r_{ab}^2 dr_{ab} R_L^2(r_{ab}) . \quad (5.7)$$

These quantities can be related to spectroscopic factors and give the total S- and D-state fractions. All the results presented here are obtained from the Argonne v_{18} two-nucleon and Urbana model IX three-nucleon interactions.

A. $\vec{d}\vec{p}$ Distribution in ${}^3\text{He}$

The calculated $R_0(r_{dp})$ and $R_2(r_{dp})$ are shown in Fig. 14; the $R_2(r_{dp})$ is negative and smaller in magnitude than the R_2 in deuteron (Fig. 2). The D_2^{dp} value obtained with these radial functions is $-0.15 \pm 0.01 \text{ fm}^2$, a little smaller than experimental estimates, ranging from -0.20 ± 0.04 to -0.25 ± 0.04 , obtained through DWBA analysis of $(d, {}^3\text{He})$ transfer reactions [46]. In Fig. 14 we also show our asymptotic fit to the S- and D-waves. The result is $\eta_{dp} = -0.035$, somewhat smaller than the Faddeev result [47], -0.043 ± 0.001 . Experimental estimates, also obtained through DWBA analysis of $(d, {}^3\text{He})$ transfer reactions, range from -0.042 ± 0.007 to -0.035 ± 0.006 [46].

The total normalizations are $N_0^{dp} = 1.31$ and $N_2^{dp} = 0.022$. The sum, 1.33, can be interpreted as the number of deuterons in ${}^3\text{He}$ [45]. It is less than 1.49 (Table I), the number of $T, S = 0, 1$ pairs, because the pairs are not always in the deuteron state. It is also smaller than $R_{Ad} = 2.0$ inferred from short range distribution functions (Fig. 13 and Table I). This is probably because ${}^3\text{He}$ is more compact than the deuteron.

The $\rho_{dp}^{0, \frac{1}{2}, \frac{1}{2}}$ and $\rho_{dp}^{1, -\frac{1}{2}, \frac{1}{2}}$ are shown in Figs. 15 and 16. When $M_d = 0$, the $M_p = +\frac{1}{2}$ proton is preferentially along the z -axis; in contrast, when $M_d = 1$, the $M_p = -\frac{1}{2}$ proton is more likely to be in the xy plane. In the first density distribution the S- and D- wave amplitudes interfere constructively, to enhance the probability of finding the proton along the z -axis, whereas in the latter the interference is constructive on the transverse xy -plane. Consequently R_0 and R_2 have opposite signs and D_2^{dp} and η_{dp} are both negative. The spin-dependent $\vec{d}\vec{p}$ anisotropies are favored by both tensor and central forces, and lead to more compact three-body states.

The momentum distribution of dp clusters in $M_J = \frac{1}{2}$ ${}^3\text{He}$ is shown in Fig. 17 for M_d , $M_p = 0, \frac{1}{2}$ and $1, -\frac{1}{2}$ for momenta parallel and transverse to the z -axis. In PWIA the ${}^3\text{He}(e, e'\vec{p})d$ cross-section is directly related to these momentum distributions. A large spin dependence of the missing-momentum distribution for protons ejected in parallel kinematics is predicted for \mathbf{q} parallel to \hat{z} . The minimum for the momentum distribution along z -axis

for $M_p = +\frac{1}{2}$ occurs at $\sim 1.4 \text{ fm}^{-1}$, while that for $M_p = -\frac{1}{2}$ is at $\sim 2.4 \text{ fm}^{-1}$. Thus the spin asymmetry, $(n_{\uparrow} - n_{\downarrow})/(n_{\uparrow} + n_{\downarrow})$, of the protons ejected from polarized ${}^3\text{He}$ changes from ~ -1 to $+1$ as the missing momentum varies from ~ 1.4 to 2.4 fm^{-1} in parallel kinematics and PWIA. The dp momentum distribution in unpolarized ${}^3\text{He}$ has been studied at Saclay [48] up to $\sim 2.5 \text{ fm}^{-1}$. The observed distribution is generally smaller than the PWIA prediction [35] indicating attenuation due to FSI. However, a part of the FSI attenuation will cancel in the asymmetry, and moreover, it is now possible to perform continuum Faddeev calculations [49] including FSI.

B. $\vec{d}\vec{d}$ Distribution in ${}^4\text{He}$

The calculated $R_0(r_{dd})$ and $R_2(r_{dd})$ are shown in Fig. 18. The D_2^{dd} value obtained with these radial functions is $-0.12 \pm 0.01 \text{ fm}^2$. In Fig. 18 we also show our asymptotic fit to the S- and D-waves. The result is $\eta_{dd} = -0.091$. The integrals of these functions yield $N_0^{dd} = 0.98$ and $N_2^{dd} = 0.024$. The number of deuterons present is greater than twice the sum of these quantities, 2.0, when one allows for the additional presence of $d + p + n$ configurations. The $\rho_{dd}^{0,0,0}$ and $\rho_{dd}^{1,-1,0}$ are large in ${}^4\text{He}$ and their anisotropies, induced by the tensor interaction and the shapes of deuterons, are shown in Fig. 19. The $\rho_{dd}^{0,0,0}$ is largest when r_{dd} is along the z -axis, i.e., when the deuterons are in the toroidal shape and have a common axis. It is smallest when \mathbf{r}_{dd} is transverse (two tori side by side) and equal to that for $\rho_{dd}^{1,-1,0}$ with \mathbf{r}_{dd} parallel to \hat{z} (two dumbbells in a line). The latter distribution is of intermediate strength when \mathbf{r}_{dd} is transverse (two dumbbells side by side). Again in the first (second) density distribution the S- and D-wave amplitudes interfere constructively (destructively) along the \hat{z} -axis. Therefore R_0 and R_2 have opposite signs and D_2^{dd} and η_{dd} are both negative.

The momentum distributions are also anisotropic (Fig. 20). In particular the $\tilde{\rho}_{dd}^{0,0,0}(k\hat{z})$ has a dip at $k \sim 1.7 \text{ fm}^{-1}$ that is absent in the $\tilde{\rho}_{dd}^{1,-1,0}(k\hat{z})$. It may be possible to study these with $(e, e'\vec{d})$ reactions. The unpolarized ${}^4\text{He}(e, e'd)d$ reaction has been studied at NIKHEF [50]. The observed cross sections are much smaller than estimates using the dd

momentum distribution and either PWIA or DWIA.

C. αd Distribution in ${}^6\text{Li}$

The calculated $R_0(r_{\alpha d})$ and $R_2(r_{\alpha d})$ are shown in Fig. 21. The $R_0(r_{\alpha d})$ and $R_2(r_{\alpha d})$ both exhibit nodes at short distances and have opposite signs almost everywhere. This nodal structure has been predicted in $\alpha + d$ and $\alpha + p + n$ cluster models, but not always with the correct relative sign [51]. The asymptotic behavior is correlated with the quadrupole moment Q ; obtaining the experimental value of -0.08 fm^2 has been a long-standing problem in $\alpha + p + n$ cluster models. The variational wave function used here gives $Q = -0.8 \pm 0.2 \text{ fm}^2$, i.e., the correct sign but far too large in magnitude. Small changes in the long range part of the ${}^6\text{Li}$ wave function have effects of order 1 fm^2 on the quadrupole moment. Thus the values of the asymptotic properties, $D_2^{\alpha d} = -0.29 \text{ fm}^2$ and $\eta_{\alpha d} = -0.07 \pm 0.02$, obtained with this wave function may not be very accurate. The total normalizations are $N_0^{\alpha d} = 0.82$ and $N_2^{\alpha d} = 0.021$. The resulting spectroscopic factor, 0.84, is in good agreement with the value of 0.85 obtained in radiative capture experiments [52].

The two-cluster densities $\rho_{\alpha d}^{0, M_d, M_J}(\mathbf{r})$, multiplied by r^2 , are shown in Fig. 22. They have two peaks; the smaller inner peak at $r \sim 0.9 \text{ fm}$ is almost spherically symmetric, while the larger peak at $r \sim 4 \text{ fm}$ is anisotropic. In particular $\rho_{\alpha d}^{0,0,0}(r\hat{z})$ is much larger than $\rho_{\alpha d}^{0,0,0}(r\hat{x})$ for $r > 2 \text{ fm}$. In the former configuration the r is along the axis of the torus, while in the latter it is transverse. This anisotropy is also a consequence of the toroidal shape of the deuteron in the $M_d=0$ state.

VI. OTHER T, S CHANNELS

In this section we discuss the properties in nuclei of pairs of nucleons with $T, S = 0, 0$, $1, 0$, and $1, 1$. Like the $T, S = 0, 1$ channel discussed in the previous sections, the $T, S = 1, 1$ channel also has a tensor potential, but it has the opposite sign of that for $T, S = 0, 1$. Therefore the role of M_S is reversed compared to that in $T = 0$ states; $M_S = 0$ pairs have

maximum density along the z -axis, while $M_S = \pm 1$ pairs have maximum density in the xy plane as can be seen in Fig. 23, which shows $\rho_{1,1}^{M_S}(r, \theta)/R_{1,1}^A$ for ${}^4\text{He}$, ${}^6\text{Li}$, and ${}^{16}\text{O}$. The curves for $M_S = \pm 1$, $\theta = \pi/2$ are between the two sets of curves shown in the figure; to reduce clutter they are not shown. The curves for ${}^4\text{He}$ and ${}^6\text{Li}$ have been renormalized by the factors $R_{1,1}^A$ to have the same peak height as for ${}^{16}\text{O}$; these factors are shown in Table II. We see that the shapes of the $T, S = 1, 1$ density profiles are quite different in the different nuclei and that the anisotropy decreases as the number of nucleons increases.

The analog of the deuteron in the $T, S = 1, 0$ channel is the ${}^1\text{S}_0$ virtual bound state (VBS). For the Argonne v_{18} potential, this is a pole on the second energy sheet at $E = -0.098$ MeV or $k = -0.049i$ fm $^{-1}$. Although the wave function is not normalizable, it has a local peak which we scale to compare to the unpolarized deuteron in Fig. 24. We see that it peaks at a slightly larger radius and is broader. The figure also shows the $\rho_{1,0}^0(r)/R_{1,0}^A$ of ${}^4\text{He}$, ${}^6\text{Li}$, and ${}^{16}\text{O}$; the curve for ${}^3\text{He}$ is between those of ${}^4\text{He}$ and ${}^6\text{Li}$, while the curve for ${}^7\text{Li}$ is very close to that of ${}^6\text{Li}$. Again the curves have been normalized to the peak height of the ${}^{16}\text{O}$ density. We see that the short-range shapes of the $\rho_{1,0}^0$ in nuclei are well reproduced by the VBS density. Finally, Fig. 25 shows the densities for the $T, S = 0, 0$ channel, again normalized to ${}^{16}\text{O}$. As is the case for $T, S = 1, 1$, there is no common shape.

Table II also shows the number of pairs, $N_{T,S}^A$, in these T, S channels and the corresponding IP values. As is the case for $T, S = 0, 1$ (Table I), the number of pairs increases more rapidly with A than does $R_{T,S}^A$, because of the increasing proportion of pairs with large separation.

Using the projection operators $(1 - \boldsymbol{\tau}_i \cdot \boldsymbol{\tau}_j)/4$ and $(3 + \boldsymbol{\tau}_i \cdot \boldsymbol{\tau}_j)/4$ for $T = 0$ and 1 pairs we find that the total number of $T = 0$ and 1 pairs in a nucleus depends only on its mass number A and isospin T_A :

$$N_{0,0}^A + N_{0,1}^A = \frac{1}{8} \left[A^2 + 2A - 4T_A(T_A + 1) \right], \quad (6.1)$$

$$N_{1,0}^A + N_{1,1}^A = \frac{1}{8} \left[3A^2 - 6A + 4T_A(T_A + 1) \right]. \quad (6.2)$$

The above relations are obeyed by $N_{T,S}^A$ obtained from either the IP or correlated wave

functions, since, in the present study, both are eigenstates of T_A .

If the total spin,

$$\mathbf{S}_A = \sum_i \frac{1}{2} \boldsymbol{\sigma}_i, \quad (6.3)$$

were to be a good quantum number we would have similar relations,

$$N_{0,0}^A + N_{1,0}^A = \frac{1}{8} [A^2 + 2A - 4S_A(S_A + 1)], \quad (6.4)$$

$$N_{0,1}^A + N_{1,1}^A = \frac{1}{8} [3A^2 - 6A + 4S_A(S_A + 1)], \quad (6.5)$$

for the total number of pairs with spin 0 and 1. They are obeyed by the $N_{T,S}^A$ calculated for the IP states which have $S_A = 1, \frac{1}{2}, 0, 1, \frac{1}{2}$ and 0 for ${}^2\text{H}$, ${}^3\text{He}$, ${}^4\text{He}$, ${}^6\text{Li}$, ${}^7\text{Li}$ and ${}^{16}\text{O}$ respectively. However, S_A is not a good quantum number; tensor correlations admix states with larger S_A in the ground state. These reduce the $N_{1,0}^A$ and increase the $N_{1,1}^A$ by the same amount due to Eq. (6.2). In ${}^3\text{He}$ (${}^4\text{He}$) the $N_{1,1}^A$ is given by $1.5P_D$ ($3P_D$), where P_D is the fraction of $L = 2$, $S_A = \frac{3}{2}$ ($S_A = 2$) state in the nuclear ground state.

The interaction in the $T, S = 1, 0$ state is much more attractive than that in the $T, S = 1, 1$ state. Hence the depletion of $T, S = 1, 0$ pairs by tensor correlations reduces the binding energy of nuclei significantly. For example, in ${}^4\text{He}$ the $T, S = 1, 0$ interaction gives -14.2 MeV per pair, while the $T, S = 1, 1$ interaction gives only -0.8 MeV per pair. Thus the conversion of 0.47 $T=1$ pairs from $S=0$ to $S=1$ state raises the energy of ${}^4\text{He}$ by ~ 6.3 MeV. It should be stressed that this is a ‘‘many-body’’ effect absent in the two-body cluster approximation of either Brueckner or variational methods. The tensor interaction between nucleons i and j can flip their spins and convert pairs ik and/or jl from $S=0$ to $S=1$.

VII. CONCLUSIONS

The main conclusions of this study of nuclear structure, as predicted by realistic models of nuclear forces, are:

(i) The static part of the two-nucleon potential in $T, S, M_S = 0, 1, 0$ state has a large angular dependence due to the tensor interaction dominated by one-pion exchange. At

$r \sim 1$ fm the difference between this potential at $\theta = \pi/2$ and 0 is ~ 300 MeV in most models (Fig. 1). It confines $T, S, M_S = 0, 1, 0$ pairs to the small θ region producing toroidal distributions. The central hole in these tori is due to the repulsive core in NN interaction. The maximum density in the tori is large, due to which the peak one-body density in deuterium exceeds 0.3 fm^{-3} in most models.

(ii) The more familiar dumbbell (or cigar) shaped density distribution of the deuteron in $M_S = \pm 1$ states can be considered as that produced by a rotating torus.

(iii) The diameter of the maximum density torus, and the thickness of the half-maximum density torus are predicted to be ~ 1.0 and 0.9 fm, respectively; these values are supported by the observed elastic electron-deuteron scattering.

(iv) The pair distribution functions in $T, S = 0, 1$ states indicate that the tensor correlations have near maximal strength in all nuclei considered here for $r \leq 2$ fm.

(v) The pair distribution functions in $T, S = 0, 1$ and $1, 0$ states in different nuclei, can be scaled to lie on universal surfaces for $r \leq 2$ fm. These universal surfaces are predicted by the density distributions of the deuteron and the 1S_0 virtual bound state. The scaling factor R_{Ad} for the $T, S = 0, 1$ densities provides a rigorous definition of the Levinger-Bethe quasi-deuteron number of the nucleus. The calculated values of R_{Ad} are significantly different from estimates based on independent-particle models, and in qualitative agreement with photon and pion absorption data.

(vi) The many-body distribution functions are also predicted to be anisotropic. In particular the anisotropies of the $\vec{d}\vec{p}$, $\vec{d}\vec{d}$, and $\alpha\vec{d}$ distributions in ^3He , ^4He and ^6Li are strongly influenced by the toroidal structure of the deuteron.

(vii) Tensor correlations convert $T=1$ pairs of nucleons from $S=0$ to $S=1$ state. This many-body effect reduces the binding energies of nuclei. It does not appear as if many-body effects reduce the magnitude of tensor correlations for the range of nuclei studied here: ^2H to ^{16}O .

Due to the small size of this toroidal structure it may be worthwhile to attempt to understand it from the more basic quark degrees of freedom. Within the constituent quark

model [54,55] it requires a solution of the six-quark problem with a suitably chosen Hamiltonian. Many attempts have been made (see Refs. [56–58] for example) to calculate the nucleon-nucleon interaction from approximate solutions of the six-quark Hamiltonian. A direct coupling of the pions to the quarks is used to obtain the tensor part of the interaction. The toroidal structure is presumably very sensitive to this coupling and to the tensor part of the quark-quark interaction in the framework of the constituent quark model.

As is well known, toroidal structure for the ground state of the deuteron was predicted many years ago [16,17] using classical Skyrme field theory [15] related to QCD in the $N_c \rightarrow \infty$ limit. In the classical limit one obtains a toroidal shape of ~ 1 fm in size and a binding energy of ~ 150 MeV. From Fig. 1 it is obvious that in the classical limit realistic models of nuclear forces would also give a deuteron binding energy in the 100 to 200 MeV range. There have been attempts to include quantum corrections to this theory. A recent calculation [18] obtains an energy of -6.18 MeV for the deuteron in this model. Ground states of the classical Skyrme field with baryon numbers 3 to 6 have also been studied [19]. The baryon equidensity surfaces of these classical solutions are highly anisotropic. However, the nucleon equidensity surfaces of the $J^\pi = \frac{1}{2}^+$ and 0^+ ${}^3\text{He}$ and ${}^4\text{He}$ must be spherically symmetric, thus a direct comparison is not possible. Nevertheless the anisotropic $\vec{d}\vec{p}$ and $\vec{d}\vec{d}$ distributions in ${}^3\text{He}$ and ${}^4\text{He}$ may have some relation to the baryon density distributions in the Skyrme model.

ACKNOWLEDGMENTS

The authors wish to thank Brian Pudliner for many interesting discussions. A.A. wishes to thank A. M. Eiró for useful discussions on the two-cluster overlap functions. R.B.W. wishes to thank Dieter Kurath for useful comments on constructing wave functions for ${}^6,7\text{Li}$. The calculations were made possible by grants of computer time from the Mathematics and Computer Science Division of Argonne National Laboratory, the Pittsburgh Supercomputing Center, the Cornell Theory Center and the National Energy Research Supercomputer Center. The work of J.L.F, V.R.P. and A.A. has been partially supported by U.S. National

Science Foundation via Grant No. Phy94-21309, that of S.C.P. and R.B.W. by the U.S. Department of Energy, Nuclear Physics Division under contract No. E-31-109-ENG-38, that of A.A. by Universidade de Lisboa, Junta de Investigação Científica e Tecnológica under contract No. PBIC/C/CEN/1108/92, and that of R.S. by the U.S. Department of Energy.

REFERENCES

* Electronic address: j-forest@uiuc.edu

† Electronic address: vijay@rsm1.physics.uiuc.edu

‡ Electronic address: spieper@anl.gov

§ Electronic address: wiringa@theory.phy.anl.gov

¶ Electronic address: schiavilla@cebaf.gov

** Electronic address: arriaga@alf1.cii.fc.ul.pt

- [1] G. van der Steenhoven and P. K. A. deWitt Huberts, in *Modern Topics in Electron Scattering*, Ed. B. Frois and I. Sick, World Scientific, p. 510 (1993).
- [2] V. R. Pandharipande, Nucl. Phys. **A553**, 191c (1993).
- [3] R. V. Reid, Jr., Ann. Phys. (N.Y.) **50**, 411 (1968).
- [4] M. Lacombe, B. Loiseau, J. M. Richard, R. Vinh Mau, J. Côté, P. Pirès, and R. de Tournel, Phys. Rev. C **21**, 861 (1980).
- [5] I. E. Lagaris and V. R. Pandharipande, Nucl. Phys. **A359**, 331 (1981).
- [6] R. B. Wiringa, V. G. J. Stoks, and R. Schiavilla, Phys. Rev. C **51**, 38 (1995).
- [7] B. S. Pudliner, V. R. Pandharipande, J. Carlson, and R. B. Wiringa, Phys. Rev. Lett. **74**, 4396 (1995).
- [8] B. S. Pudliner, Ph.D. Thesis, University of Illinois at Urbana-Champaign, 1996.
- [9] A. Arriaga, V. R. Pandharipande, and R. B. Wiringa, Phys. Rev. C **52**, 2362 (1995).
- [10] R. B. Wiringa, S. C. Pieper, and B. S. Pudliner, in preparation.
- [11] S. C. Pieper, R. B. Wiringa, and V. R. Pandharipande, Phys. Rev. C **46**, 1741 (1992).
- [12] S. C. Pieper, in preparation.

- [13] T. E. O. Ericson and W. Weise, *Pions and Nuclei*, Oxford University Press (1988).
- [14] J. M. Blatt and V. F. Weisskopf, *Theoretical Nuclear Physics*, John Wiley and Sons, New York (1952).
- [15] V. G. Makhankov, Y. P. Rybakov and V. I. Sanyuk, *The Skyrme Model*, Springer-Verlag (1993).
- [16] V. B. Kopeliovich and B. E. Stern, JETP Lett. **45**, 203 (1987).
- [17] J. J. M. Verbaarschot, T. S. Walhout, J. Wambach and H. W. Wyld, Nucl. Phys. **A468**, 520 (1987).
- [18] R. A. Leese, N. S. Manton and B. J. Schroers, Nucl. Phys. **B442**, 228 (1995).
- [19] E. Braaten, L. Carson and S. Townsend, Phys. Lett. **B235**, 147 (1990).
- [20] R. Machleidt, K. Holinde, and Ch. Elster, Phys. Rep. **149**, 1 (1987).
- [21] R. G. Arnold *et al.*, Phys. Rev. Lett. **35**, 776 (1975).
- [22] G. G. Simon, Ch. Schmitt, and V. H. Walther, Nucl. Phys. **A364**, 285 (1981).
- [23] R. Cramer *et al.*, Z. Phys. C **29**, 513 (1985).
- [24] S. Platchkov *et al.*, Nucl. Phys. **A510**, 740 (1990).
- [25] S. Auffret *et al.*, Phys. Rev. Lett. **54**, 649 (1985).
- [26] R. G. Arnold *et al.*, Phys. Rev. Lett. **58**, 1723 (1987).
- [27] M. E. Schulze *et al.*, Phys. Rev. Lett. **52**, 597 (1984).
- [28] I. The *et al.*, Phys. Rev. Lett. **67**, 173 (1991).
- [29] V. F. Dmitriev *et al.*, Phys. Lett. **157B**, 143 (1985).
- [30] R. Gilman *et al.*, Phys. Rev. Lett. **65**, 1733 (1990).

- [31] W. Fabian and H. Arenhövel, Nucl. Phys. **A258**, 461 (1976).
- [32] E. Hummel and J. A. Tjon, Phys. Rev. Lett. **63**, 1788 (1989).
- [33] R. Schiavilla and D. O. Riska, Phys. Rev. C **43**, 437 (1991).
- [34] J. W. Van Orden, N. Devine, and F. Gross, Phys. Rev. Lett. **75**, 4369 (1995).
- [35] J. M. Laget, in *Modern Topics in Electron Scattering*, Ed. B. Frois and I. Sick, World Scientific, p. 290 (1991).
- [36] J. S. Levinger, *Nuclear Photo-disintegration*, Oxford University Press (1960).
- [37] T. Altholz *et al.*, Phys. Rev. Lett. **73**, 1336 (1994).
- [38] A. O. Mateos, Ph.D Thesis, Massachusetts Institute of Technology, 1995.
- [39] D. J. Mack *et al.*, Phys. Rev. C **45**, 1767 (1992).
- [40] J. Ahrens, Nucl. Phys. **A446**, 229c (1985).
- [41] D. A. Jenkins, P. T. Debevec, P. D. Harty, Phys. Rev. C **50**, 74 (1994).
- [42] V. N. Fetisov, A. N. Gorbunov, and A. T. Varfolomeev, Nucl. Phys. **71**, 305 (1965).
- [43] N. M. O'Fallon, L. J. Koester Jr., and J. H. Smith, Phys. Rev. C **5**, 1926 (1972).
- [44] Y. M. Arkatov *et al.*, Sov. J. Nucl. Phys. **31**, 726 (1980).
- [45] R. Schiavilla, V. R. Pandharipande and R. B. Wiringa, Nucl. Phys. **A449**, 219 (1986).
- [46] A. M. Eiró and F. D. Santos, J. Phys. G **16**, 1139 (1990).
- [47] J. L. Friar, B. F. Gibson, D. Lehman, and G. L. Payne, Phys. Rev. C **37**, 2859 (1988).
- [48] C. Marchand *et al.*, Phys. Rev. Lett. **60**, 1703 (1988).
- [49] W. Glöckle, H. Witala and Th. Cornelius, Nucl. Phys. **A508**, 115c (1990).
- [50] R. Ent *et al.*, Nucl. Phys. **A578**, 93 (1994).

- [51] V. I. Kukulin, V. N. Pomerantsev, Kh. D. Razikov, V. T. Voronchev, and G. G. Ryzhikh, Nucl. Phys. **A586**, 151 (1995).
- [52] R. G. H. Robertson *et al.*, Phys. Rev. Lett. **47**, 1867 (1981).
- [53] R. A. Malfliet and J. A. Tjon, Nucl. Phys. **A127**, 161 (1969).
- [54] N. Isgur, in *Hadrons and Hadronic Matter*, Ed. D. Vautherin, F. Lenz and J. W. Negele, Plenum Press, New York and London (1990).
- [55] J. Carlson and V. R. Pandharipande, Phys. Rev. D **43**, 1652 (1991).
- [56] D. Robson, Phys. Rev. D **35**, 1029 (1987).
- [57] F. Fernandez, A. Valcarce, U. Straub and A. Faessler, J. Phys. G **19** 2013 (1993).
- [58] Y. W. Yu, Z. Y. Zhang, P. N. Shen and L. R. Dai, Phys. Rev.C **52**, 3393 (1993).

FIGURES

FIG. 1. The upper four lines show expectation values of $v_{0,1}^{stat.}$ for $M_S=0, \theta=0$, and the lower four lines are for $M_S=0, \theta=\pi/2$ or equivalently $M_S=\pm 1, \theta=0$. The expectation values for $M_S=\pm 1, \theta=\pi/2$ (not shown) are half way in between.

FIG. 2. The S - and D -wave deuteron wave functions for various potential models.

FIG. 3. The top, middle and bottom four curves respectively show the deuteron density for the indicated values of M_d and θ , obtained from various potential models.

FIG. 4. The deuteron density $\rho_d^0(x', z')$ obtained from the Argonne v_{18} model. The peaks are located at $z'=0$ and $x'=\pm d/2$.

FIG. 5. The deuteron density $\rho_d^{\pm 1}(x', z')$ obtained from the Argonne v_{18} model. The peaks are located at $x'=0$ and $z'=\pm d/2$.

FIG. 6. The surfaces having $\rho_d^{\pm 1}(\mathbf{r}')=0.24 \text{ fm}^{-3}$ (A) and $\rho_d^0(\mathbf{r}')=0.24 \text{ fm}^{-3}$ (B). The surfaces are symmetric about z' axis and have $r' \leq 0.74 \text{ fm}$, i.e., the length of the dumbbell along z' axis as well as the diameter of the outer surface of the torus is 1.48 fm. Sections C and D are for $\rho_d^{M_d}(\mathbf{r}')=0.08 \text{ fm}^{-3}$; the maximum value of r' is 1.2 fm.

FIG. 7. The square of the calculated deuteron charge form factors.

FIG. 8. The values of deuteron $T_{20}(q)$ obtained from Eq. (3.11) are shown by full line, whereas the dashed line gives $T_{20}(q)$ including magnetic contributions for a 15° electron scattering angle.

FIG. 9. The square of the deuteron magnetic form factor calculated with (full line) and without (dashed line) convection current term.

FIG. 10. The transition density $\rho_{tr}(x'z')$ for elastic magnetic scattering by deuterons. The peaks are located at $z'=0$ and $x'=\pm 0.5 \text{ fm}$.

FIG. 11. The deuteron momentum distribution for selected values of M_d and θ_k .

FIG. 12. The calculated values of $\vec{d}(e, e'p)n$ cross section for the kinematics described in the text. Hollow and filled symbols indicate results of complete calculations without and with meson-exchange currents.

FIG. 13. $\rho_{0,1}^{MS}(r, \theta)/R_{Ad}$ for various nuclei.

FIG. 14. $R_0(r_{dp})$ and $R_2(r_{dp})$ for ${}^3\text{He}$. The points show results of Monte Carlo calculations in configuration space, and the curves are smooth fits. The asymptotic R_L given by Eq. (5.5) are shown by dashed lines.

FIG. 15. Density distribution of dp clusters in ${}^3\text{He}$ with $M_J = \frac{1}{2}$, $M_d=0$ and $M_p = \frac{1}{2}$. The peaks are located at $x_{dp}=0$ and $z_{dp} \sim \pm 1$ fm.

FIG. 16. Density distribution of dp clusters in ${}^3\text{He}$ with $M_J = \frac{1}{2}$, $M_d=1$ and $M_p = -\frac{1}{2}$. The peaks are located at $z_{dp}=0$ and $x_{dp} \sim \pm 1$ fm

FIG. 17. Momentum distribution of \vec{dp} clusters in ${}^3\text{He}$ in $M_J = \frac{1}{2}$ state for momenta parallel and transverse to the z -axis

FIG. 18. $R_0(r_{dd})$ and $R_2(r_{dd})$ for ${}^4\text{He}$. See Fig. 15 for notation.

FIG. 19. Density distribution of \vec{dd} clusters in ${}^4\text{He}$ in parallel ($\theta=0$) and transverse ($\theta=\pi/2$) directions.

FIG. 20. Momentum distribution of \vec{dd} clusters in ${}^4\text{He}$ in parallel ($\theta=0$) and transverse ($\theta=\pi/2$) directions.

FIG. 21. $R_0(r_{\alpha d})$ and $R_2(r_{\alpha d})$ for ${}^6\text{Li}$. See Fig. 15 for notation.

FIG. 22. Density distribution of $\alpha\vec{d}$ clusters in ${}^6\text{Li}$ in parallel ($\theta=0$) and transverse ($\theta=\pi/2$) directions.

FIG. 23. $\rho_{1,1}^{M_S}(r, \theta)/R_{1,1}^A$ for various nuclei. The upper three curves are for $M_S=0, \theta=0$ while the lower ones are for $M_S=0, \theta=\pi/2$ and equivalently $M_S=\pm 1, \theta=0$.

FIG. 24. $\rho_{1,0}^0(r)/R_{1,0}^A$ for various nuclei. The $\rho(r)$ of an unpolarized deuteron, normalized to have the same maximum value, is shown for comparison by the dotted line.

FIG. 25. $\rho_{0,0}^0(r)/R_{0,0}^A$ for various nuclei.

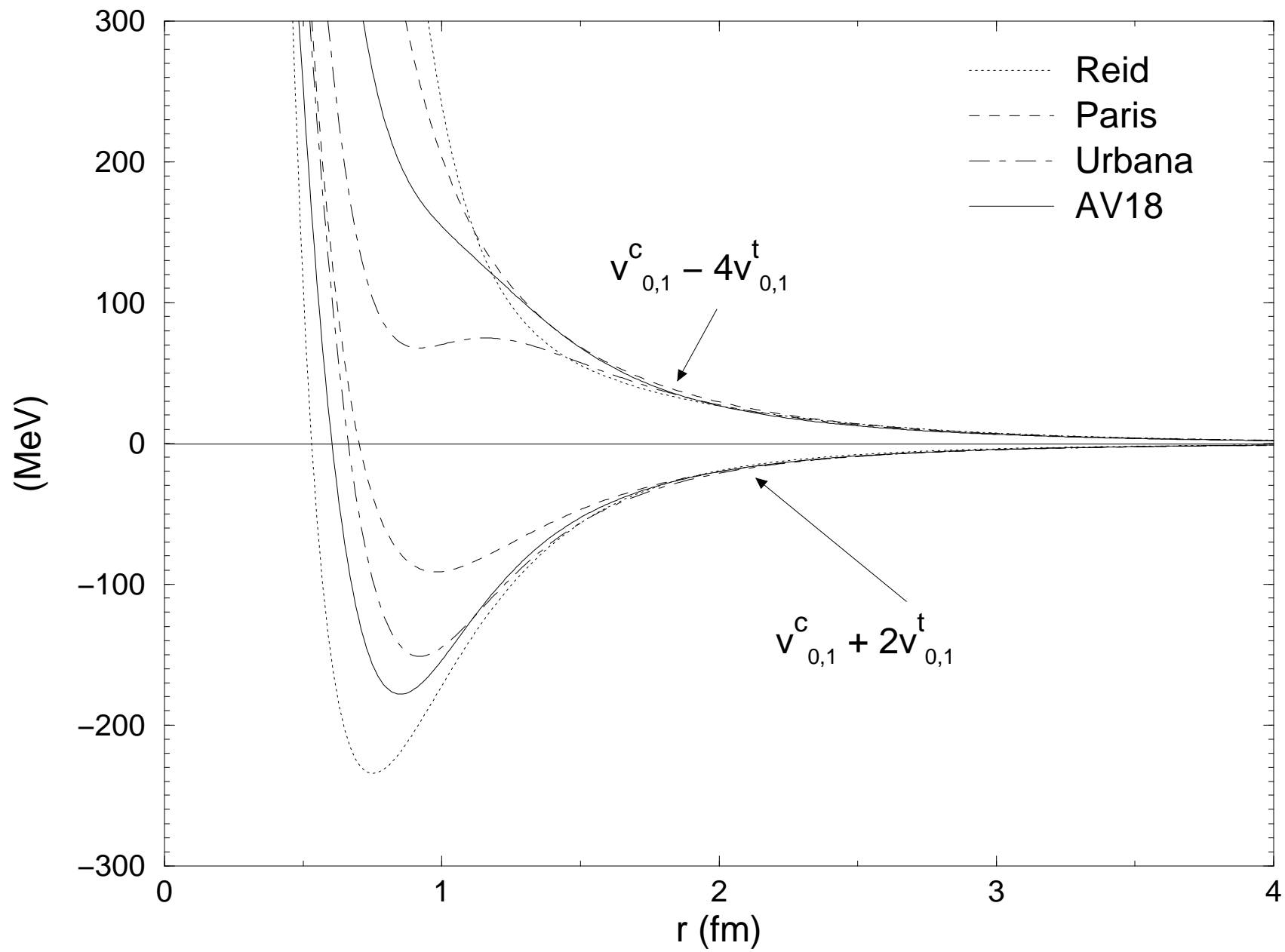
TABLES

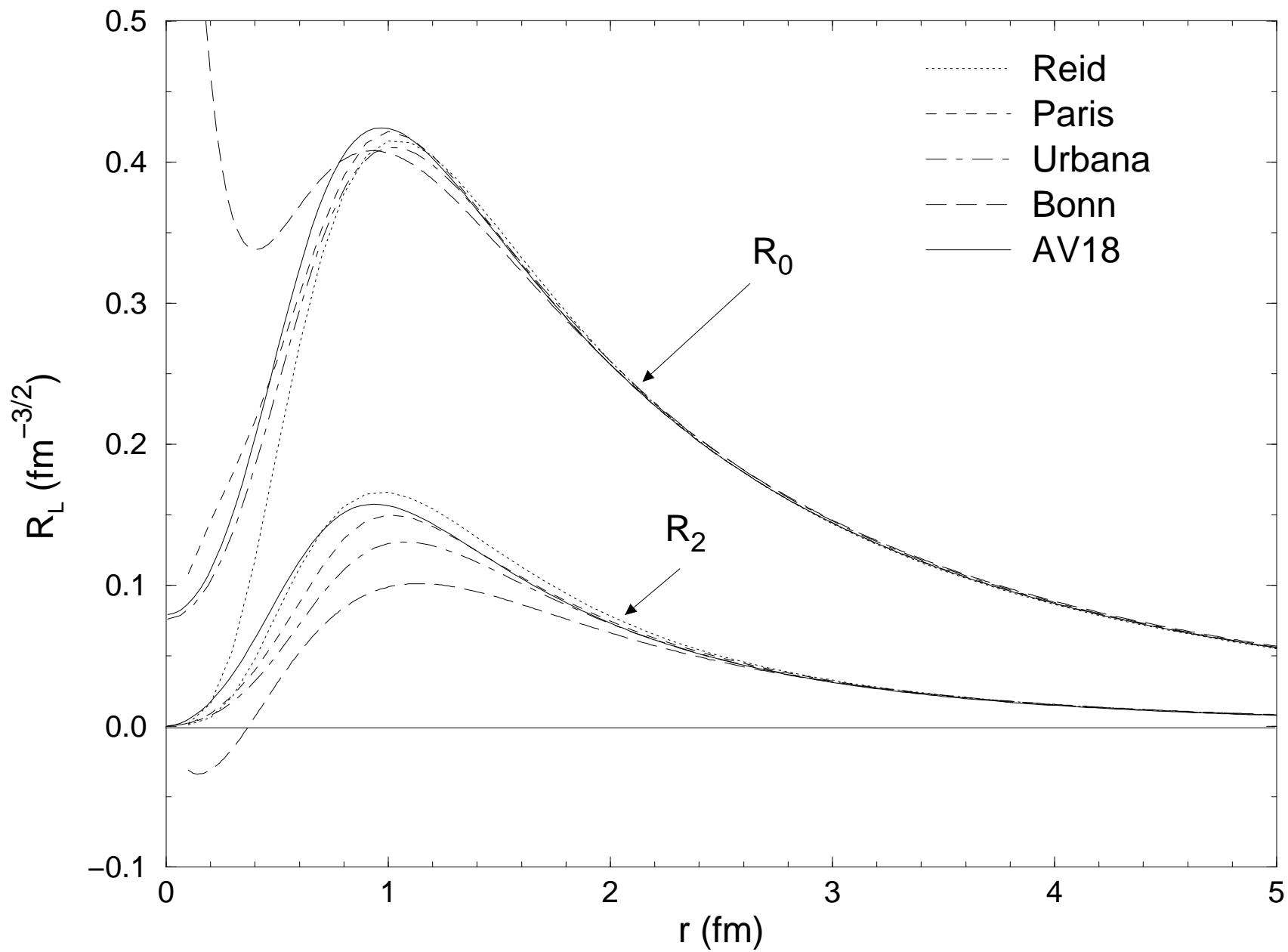
TABLE I. The calculated values of R_{Ad} and other ratios.

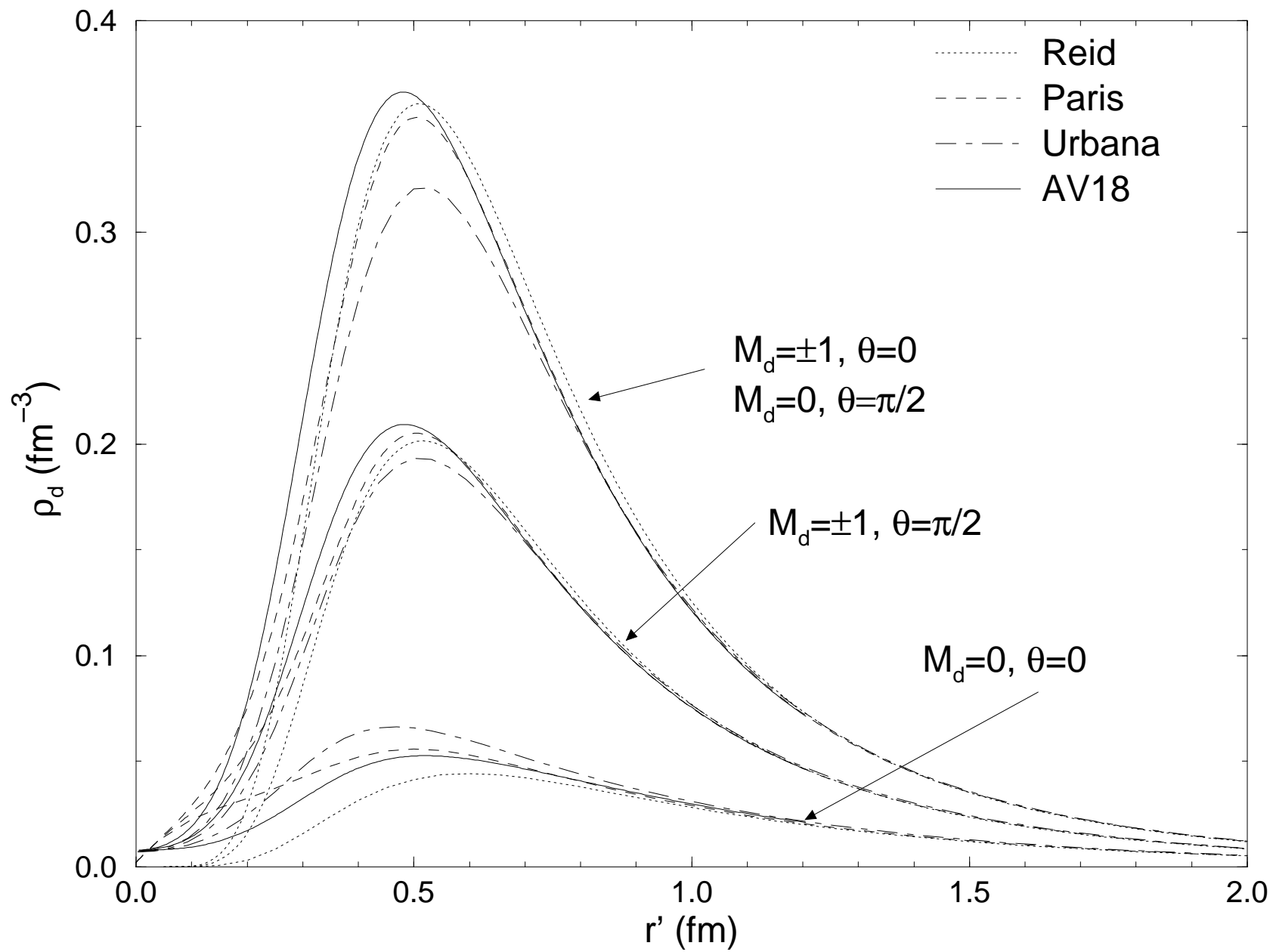
Nucleus	R_{Ad}	$\frac{\langle v_\pi \rangle_A}{\langle v_\pi \rangle_d}$	$\frac{\sigma_{ab,A}^\pi}{\sigma_{ab,d}^\pi}$	$\frac{\sigma_{ab,A}^\gamma}{\sigma_{ab,d}^\gamma}$	$N_{0,1}^A$	
					IP	Ψ_v
^3He	2.0	2.1	2.4(1)	~ 2	1.5	1.49
^4He	4.7	5.1	4.3(6)	~ 4	3	2.99
^6Li	6.3	6.3			5.5	5.46
^7Li	7.2	7.8		6.5(5)	6.75	6.73
^{16}O	18.8	22	17(3)	16(3)	30	30.1

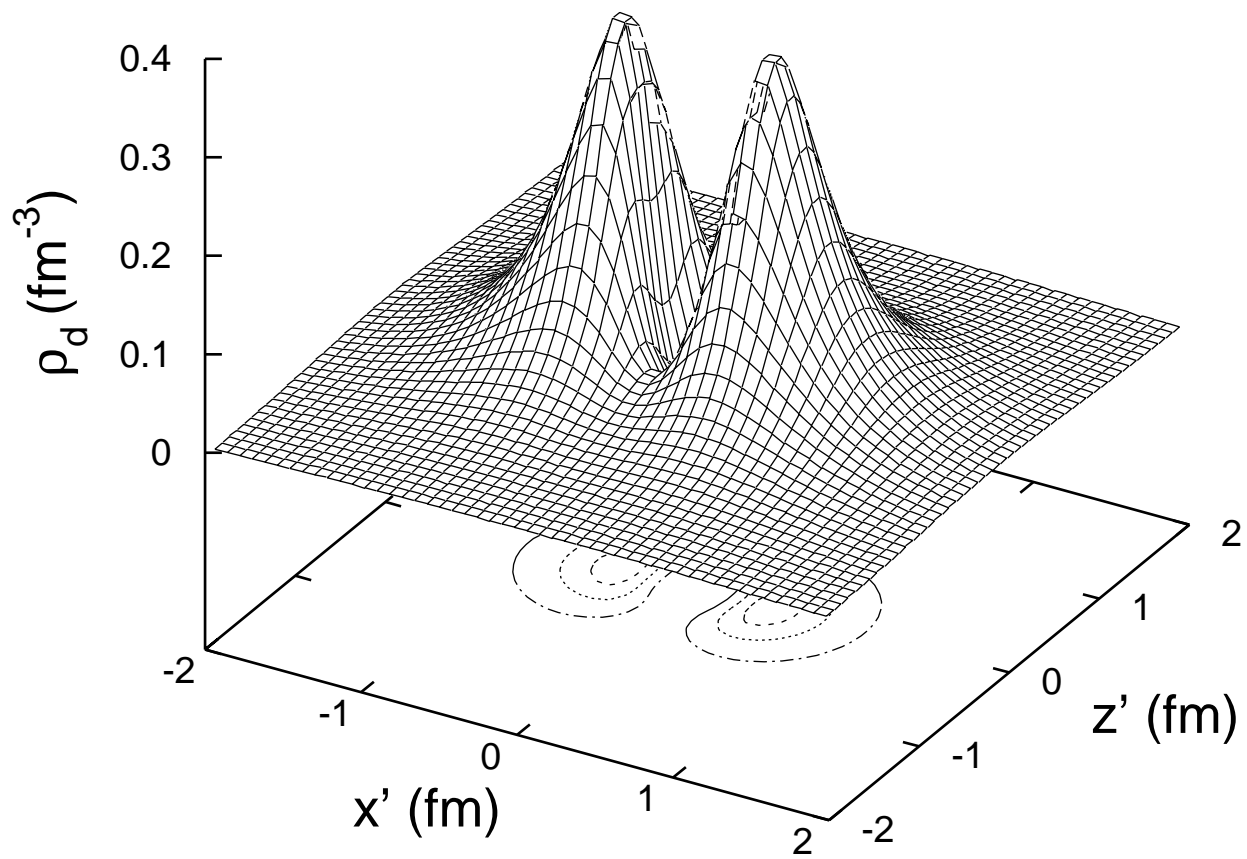
TABLE II. The calculated values of $R_{T,S}^A$ and $N_{T,S}^A$ in various nuclei.

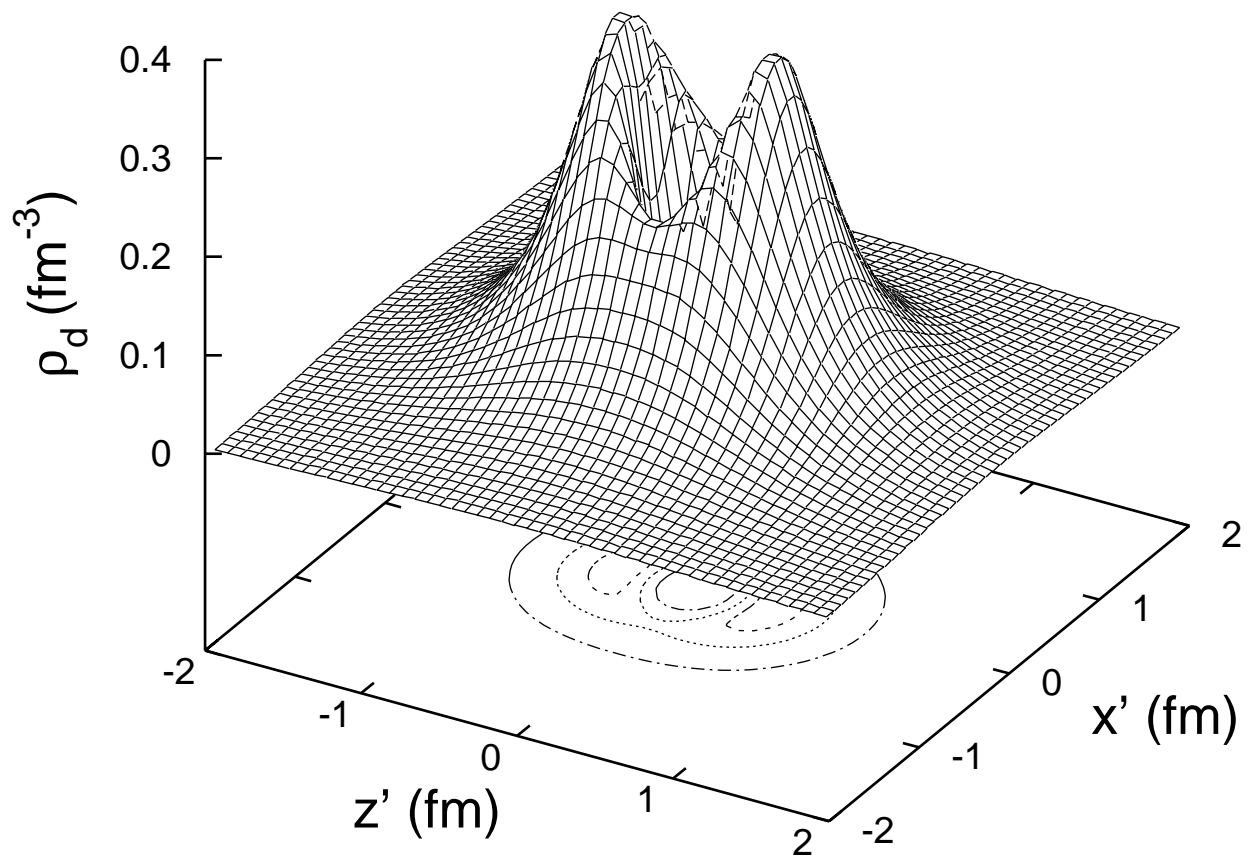
Nucleus	$R_{1,0}^A$	$N_{1,0}^A$		$R_{0,0}^A$	$N_{0,0}^A$		$R_{1,1}^A$	$N_{1,1}^A$	
		IP	Ψ_v		IP	Ψ_v		IP	Ψ_v
^3He	0.087	1.5	1.35	0.0016	0	0.01	0.012	0	0.14
^4He	0.22	3	2.5	0.0085	0	0.01	0.060	0	0.47
^6Li	0.24	4.5	4.0	0.061	0.5	0.52	0.104	4.5	4.96
^7Li	0.37	6.75	6.1	0.118	0.75	0.77	0.18	6.75	7.41
^{16}O	1	30	28.5	1	6	6.05	1	54	55.5

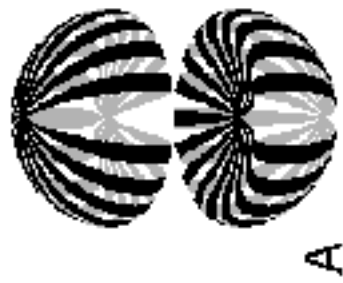




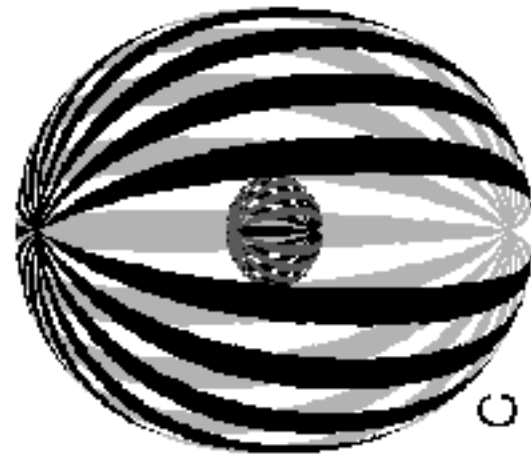








$$M_{\sigma} = \pm 1$$



$$M_{\sigma} = 0$$

